Kent Academic Repository

Downloaded from

The version of record is available from

This document version

Author's Accepted Manuscript

DOI for this version

Licence for this version

UNSPECIFIED

Additional information

Versions of research works

Versions of Record

If this version is the version of record, it is the same as the published version available on the publisher's web site. Cite as the published version.

Author Accepted Manuscripts

If this document is identified as the Author Accepted Manuscript it is the version after peer review but before type setting, copy editing or publisher branding. Cite as Surname, Initial. (Year) 'Title of article'. To be published in *Title of Journal* , Volume and issue numbers [peer-reviewed accepted version]. Available at: DOI or URL (Accessed: date).

Enquiries

Tunable Magnetism and Extraordinary Sunlight Absorbance in Indium Triphosphide Monolayer

Naihua Miao,[†,‡] Bin Xu,[¶] Nicholas C. Bristowe,[§] Jian Zhou,[†] and Zhimei Sun[*,†,‡]

†*School of Materials Science and Engineering, Beihang University, Beijing, 100191, China.*
‡*Center for Integrated Computational Materials Engineering, International Research Institute for Multidisciplinary Science, Beihang University, Beijing, 100191, China.*
¶*Physics Department and Institute for Nanoscience and Engineering, University of Arkansas, Fayetteville, Arkansas, 72701, USA.*
§*School of Physical Sciences, University of Kent, Canterbury, CT2 7NH, United Kingdom.*

E-mail: zmsun@buaa.edu.cn

Phone: +86-(0)10-82317747. Fax: +86-(0)10-82317747

1

Abstract

Atomically thin two-dimensional (2D) materials have received considerable research interest due to their extraordinary properties and promising applications. Here we predict the mono-layered indium triphosphide (InP_3) as a new semiconducting 2D material with a range of favourable functional properties by means of *ab initio* calculations. The 2D InP_3 crystal shows high stability and promise of experimental synthesis. It possesses an indirect band-gap of 1.14 eV and a high electron mobility of 1919 $cm^2V^{-1}s^{-1}$, which can be strongly manipulated with applied strain. Remarkably, the InP_3 monolayer suggests tunable magnetism and half-metallicity under hole doping or defect engineering, which is attributed to the novel Mexican-hat-like bands and van Hove singularities in its electronic structure. A semiconductor-metal transition is also revealed by doping 2D InP_3 with electrons. Furthermore, mono-layered InP_3 exhibits extraordinary optical absorption with significant excitonic effects in the entire range of the visible-light spectrum. All these desired properties render 2D InP_3 a promising candidate for future applications in a wide variety of technologies, in particular for electronic, spintronic and photovoltaic devices.

INTRODUCTION

Since the discovery of graphene,[1–3] one-atom-thick mono-layered two-dimensional (2D) nano-materials have received unparalleled attention owing to their rich phenomena, exceptional properties, and promising applications in nanoscale devices.[1,4–13] The family of 2D nanomaterials is growing rapidly, including silicene,[14,15] germanane,[14] phosphorus allotropes,[12,16,17] MXenes,[18–20] and transition-metal chalcogenides.[7,21–25] To date, their potential applications in field-effect transistors, light-emitting devices, photovoltaic solar cells, and photocatalysts have been studied intensively. However, inducing and controlling magnetism in 2D crystals remains a challenge despite various proposed strategies, and new 2D materials with tunable magnetic properties and half-metallicity are still in high demand for spintronic devices.[7,26,27] In addition, 2D crystals with band-gap and optical properties comparable to silicon ($\sim$1.16 eV) are still highly sought for efficient photovoltaic and optoelectronic applications,[28,29] which requires sufficiently large (10^5 cm^{-1}) absorption coefficients covering the entire visible light wavelengths from 380 to 750 nm. To this end, the search for new 2D semiconductors with desirable electronic and optical properties for photovoltaic solar cells is of great interest.

Numerous 2D nanomaterials have been readily exfoliated from their bulk crystals with van der Waals (vdW) bonding between adjacent layers and exhibit exceptionally different properties from their bulk courparts.[1,30] As a layered compound of the In-P system, indium triphosphide (InP$_3$) was prepared under pressure in the 1980s and it can be quenched to ambient conditions.[31] With a space group of $R\bar{3}$m, the structure of InP$_3$ (Figure 1) is closely related to that of arsenic, replacing systematically every fourth atom in the arsenic layer by an indium atom and the rest by phosphorous.[32] The layers stack on one another along the c-axis with vdW bonds. Compared to other layered nanomaterials which have been cleaved from their bulk crystals, one might therefore expect the fabrication of InP$_3$ monolayers to also be possible. However, it is surprising that InP$_3$ monolayers are yet to be prepared, and that a comprehensive understanding of the monolayer form is still lacking.

In this work, using *ab initio* density functional calculations and molecular dynamics sim-

ulations, we identify the mono-layered InP$_3$ as a new 2D semiconductor. We first investigate comprehensively the electronic properties of the InP$_3$ monolayer, both free-standing and under applied strain. Then we show that the magnetic properties and half-metallicity of 2D InP$_3$ crystal can be tuned by carrier doping and defect engineering (*i.e.*, doped with Ge). Furthermore, we present optical absorption coefficients in comparison with intrinsic silicon and mono-layered MoS$_2$, and discuss potential applications of this new 2D semiconductor in optoelectronics, spintronics, as well as photovoltaics. Finally, we assess the lattice dynamical and thermal stability of this new 2D crystal according to the calculated phonon dispersion curves and molecular dynamics trajectories. The potential experimental approach and feasibility to prepare 2D InP$_3$ from its bulk form are proposed and explored as well.

COMPUTATIONAL METHODOLOGY

Within the framework of density functional theory (DFT), all calculations were performed using a projector-augmented wave method[33] as implemented in the Vienna *ab initio* Simulation Package (VASP).[34] The valence electron configurations are $3s^23p^3$ for P, $5s^25p$ for In, and $4s^24p^2$ for Ge, respectively. The generalized gradient approximation with Perdew-Burke-Ernzerhof parametrization (GGA-PBE)[35] was applied as the exchange-correlation functional and the density functional dispersion correction (D3-Grimme)[36] was adopted for a better description of the van der Waals interactions between layers. A cut-off energy of 400 eV was set for the plane wave basis. The convergence criteria were 1×10^{-2} eV/Å for the residual forces on ions and 1×10^{-6} eV for the energy difference in electronic self-consistent loop. Γ-centred k-meshes of $7\times7\times5$ and $7\times7\times1$ were used for bulk and mono-layered unit-cells, respectively. To minimize the interlayer interactions under the periodic boundary condition, a vacuum of 20 Å was constructed perpendicular to the layer plane for the monolayers. Electronic band structures were obtained by GGA-PBE (unless stated otherwise) and compared with those from the Heyd-Scuseria-Ernzerhof (HSE06) screened hybrid functional.[37] The

phonon calculations were performed using a 4×4×1 supercell with the finite displacement method.[38–40]

The carrier mobility (μ) is calculated based on the deformation potential theory,[41] which has been successfully used in many 2D materials.[17,25,42,43] Accordingly, the carrier mobility in 2D materials can be expressed as $\mu = \dfrac{2e\hbar^3 C}{3k_B T |m^*|^2 E_{DP}^2}$, where C is the elastic modulus defined as $C = (\partial\varepsilon/\partial\delta) \times V_0/S_0$, in which ε is stress under the applied uniaxial strain δ and V_0/S_0 is the volume/area of the optimized 2D structure. m^* is the effective mass of electron and hole, which can be calculated from the derivatives of electronic bands.[44] E_{DP} is the deformation potential constant, defined as $\Delta E = E_{DP}(\Delta l/l_0)$, where ΔE is the shift of the band edge positions with respect to the lattice dilation $\Delta l/l_0$ along the zigzag and armchair directions of orthogonal cell. The relaxation time of carrier is estimated by $\tau = \mu m^*/e$.

To include excitonic effects, the frequency-dependent dielectric matrices were predicted using time-dependent Hartree-Fock approach (TDHF) on top of the HSE06 hybrid functional calculations.[45] Consequently, the absorption coefficients were derived from the dielectric functions:[46]

$$\alpha(\omega) = \sqrt{2}\omega[\sqrt{\varepsilon_1^2(\omega) + \varepsilon_2^2(\omega)} - \varepsilon_1(\omega)]^{1/2} \tag{1}$$

The imaginary part of the dielectric functions $\varepsilon_2(\omega)$ was obtained by summation over empty states, while the real part $\varepsilon_1(\omega)$ was calculated according to the usual Kramers-Kronig transformation.[46–48] Finally, all components of the absorption spectra and related optical quantities could be determined.

Ab initio molecular dynamics (AIMD) simulations were performed for a 4×4×1 supercell at 300 K using VASP. A canonical ensemble (NVT) with Nose-Hoover thermostat[49,50] was adopted. The total simulation lasted 10 ps with a timestep of 2 fs. During the AIMD simulations, all the ions in the cell were allowed to move away from their equilibrium positions with all degrees of freedom by removing any symmetry restrictions from the current structure and maintaining only its translational periodicity.
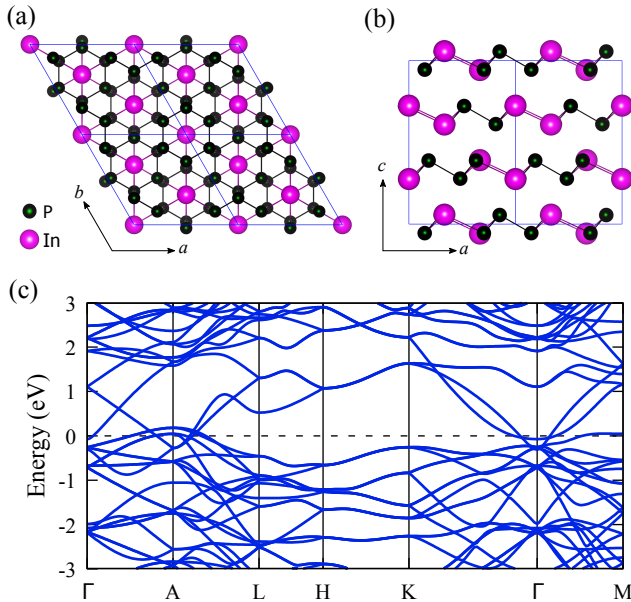
RESULTS AND DISCUSSION

Figure 1 Crystal structures of indium triphosphide: (a) top view of 2×2 planer layers from c axis and (b) side view of 2×1 supercell along b axis. (c) Calculated electronic band structure of bulk InP$_3$. The Fermi level is set at 0 eV.

Structure. Bulk indium triphosphide is a natural pseudo-two-dimensional crystal as shown in Figure 1 (a) and (b), possessing planer 2D networks of puckered arsenic-type honeycomb structure in the ab plane and van der Waals layers stacking along the c direction. The D3-Grimme optimized lattice parameters of bulk InP$_3$ are a=7.521 Å and c=9.975 Å, which are in very good agreement with the experimental data of a=7.449 Å and c=9.885 Å.[31] Excellent agreement between our calculated results and previous experiments is also observed for the internal atomic positions of the bulk crystal as summarized in Table S1 of the supporting information (SI), attesting to the reliability and accuracy of our prediction. The optimized lattice constant of InP$_3$ monolayer is 7.557 Å (also see SI for structural detail), being slightly larger than its bulk form, and the bond angles of the mono-layered and bulk formd are very different (Table S2). According to experiments, bulk InP$_3$ is a metallic conductor.[31] This is however contrary to the anticipation that it should be semiconducting, as it does not have four valence electrons to retain an electron octet on phosphorus, whereas,

6

in germanium and tin triphosphides, the fourth electron of Ge and Sn was considered to contribute to their metallic conductivity.[31,32] As shown in Figure 1 (c), the bulk crystal is metallic with electronic bands crossing the Fermi level, which is also the case for bi-layered and tri-layered counterparts (Figure S1). While the InP$_3$ monolayer is a semiconductor with an indirect band-gap, and it is the surface relaxation which opens the gap (Figure S2), but rather than the quantum confinement effect, as bond angles of the mono-layered and bulk forms are significantly different (Table S2).

Electronic Structure. Figure 2 (a) illustrates the calculated electronic band structure of 2D InP$_3$ crystal. Clearly, the InP$_3$ monolayer is an indirect band-gap semiconductor, as the conduction band minimum (CBM) is at the Γ point, while the valence band maximum (VBM) locates between the Γ and M points, which is only marginally higher in energy than the Γ point. The weakly indirect band gap might be advantageous for photovoltaics (see below), allowing simultaneously for strong absorption and long charge carrier lifetimes, as is proposed in the promising hybrid perovskites.[51] Remarkably, the calculated electronic band-gap of the monolayer is 0.62 eV from GGA-PBE and 1.14 eV using the accurate HSE06 functional, very close to experimental gap of bulk silicon ($\sim$1.16 eV),[52] which is of particular interest for photovoltaic and optoelectronic applications. It is interesting to see that the top valence bands near the Fermi level are very flat and have the shape of Mexican-hat-like bands around the Γ point, which result in high density of states and almost one-dimensional-like van Hove singularities as suggested by Figure 2 (b). The Mexican-hat-like valence bands are mostly contributed of the 3p and 5p orbitals of P and In atoms, respectively, and these orbitals are strongly overlapping in the full energy range, indicating covalent bonding characters of P-P and In-P bonds. The covalent bondings in 2D InP$_3$ crystal are further evidenced by the topological analysis of electron localization functions (ELF) in Figure 2 (c), where the ELF values of In-P and P-P bonds are all larger than 0.75, suggesting that valence electrons are shared between the neighbouring atoms.[53,54]

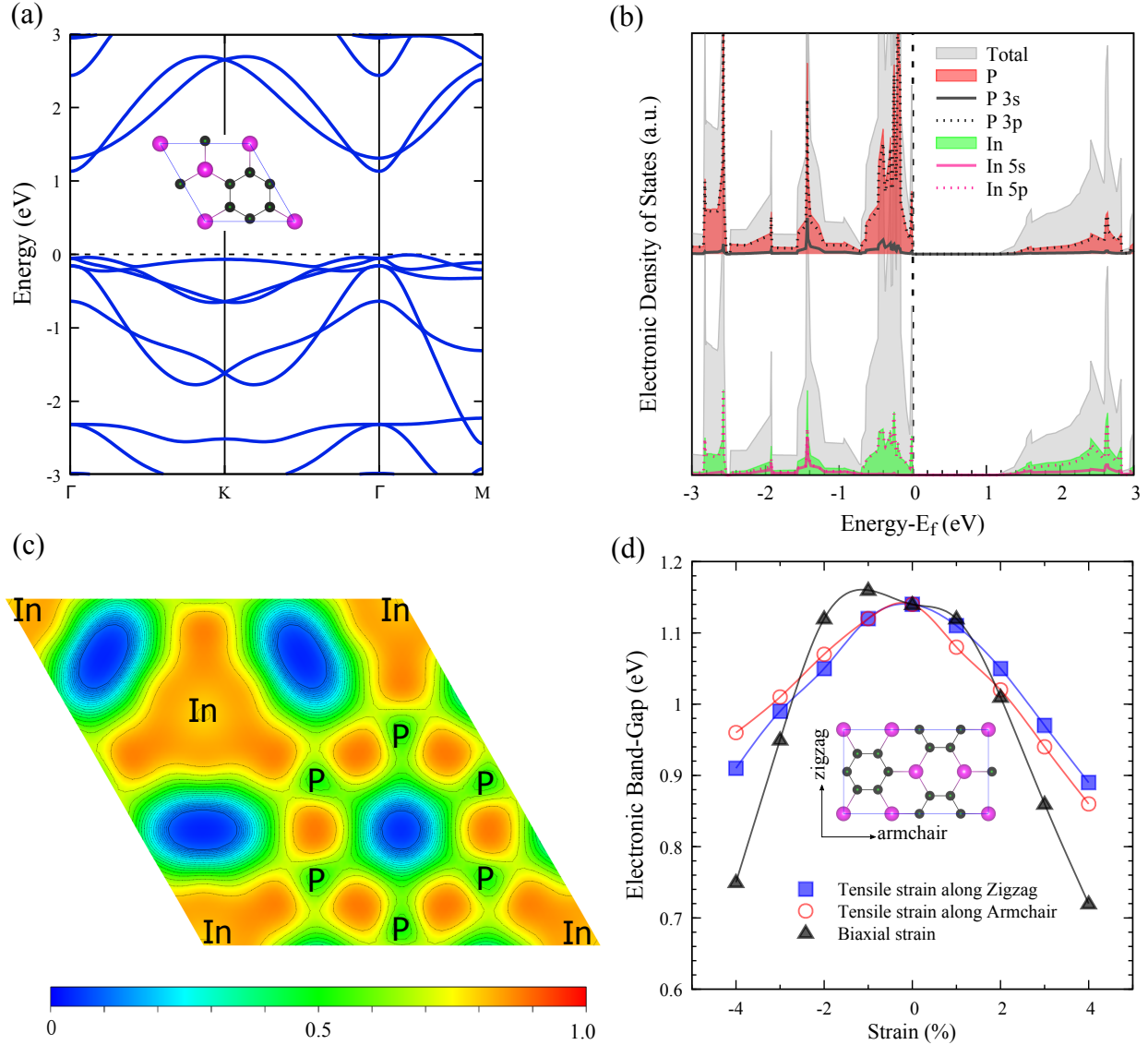One of the most effective approaches to tune the electronic structure and transport prop-

Figure 2 (a) Electronic band structure, (b) density of states, and (c) electron localization functions of the InP$_3$ monolayer. The dashed line at 0 eV indicates the Fermi energy. (d) Electronic band-gap of its orthogonal cell under various strains calculated using the HSE06 functional.

erty of bulk and 2D semiconductors is strain engineering.[30,41,55–57] The calculated electronic band-gaps of the orthogonal cell (Figure S3a) under various strains are depicted in Figure 2 (d) (and Figure S3b for band-edges). Interestingly, the band-gaps of InP$_3$ monolayer decrease gradually with either compressive or tensile strains and it does not show a monotonic trend from compression to tension of the lattice as phosphorene and many other 2D materials do.[30] This exceptional behaviour is attributed to Mexican-hat-like flat valence bands near the Fermi energy as discussed above. The one-dimensional-like electronic states result in a non-monotonic response of the VBM to various strains, rather than a monotonic behaviour as observed in the CBM (Figure S3b), which may be of interest for future application in flexible electronic devices.

Table 1 Calculated deformation-potential constant (E_{DP}), 2D in-plane stiffness (C), effective mass (m^*), carrier mobility, and relaxation time (τ) along the zigzag and armchair directions for InP$_3$ monolayer at 300 K.

Carrier type	E_{DP} (eV)	C (N/m)	m^* (m_e)	μ (cm^{2}V^{-1}s^{-1})	τ(ps)
electron (zigzag)	4.118	43.280	0.259	540	0.080
hole (zigzag)	6.618	43.280	1.536	6	0.005
electron (armchair)	2.404	42.402	0.233	1919	0.254
hole (armchair)	0.846	42.402	4.017	52	0.119

Carrier Mobility. From the electronic band structure of 2D InP$_3$, it can be clearly seen that the conduction bands are very dispersive, indicating a high electron mobility. The predicted deformation-potential constant, in-plane stiffness, effective mass, carrier mobility, and relaxation time are summarized in Table 1. Most electronic quantities of the InP$_3$ monolayer are moderately large and anisotropic along the zigzag and armchair directions of the orthogonal cell, except the 2D stiffness. The directional 2D stiffnesses are relatively isotropic, which may result from the planar puckered hex-atomic rings in the InP$_3$ monolayer. The calculated effective mass of electrons are an order of magnitude smaller than that of the holes, owing to the flat valence band and more dispersive conduction band of 2D InP$_3$, where the former also leads to extremely low hole mobilities in both directions. The greatest electron mobility of the InP$_3$ monolayer is predicted to be 1919 cm^{2}V^{-1}s^{-1} along the armchair

direction at 300 K, which is significantly higher than that of the MoS$_2$ monolayer nanosheet of ~ 400 cm^{2}V^{-1}s^{-1},[23] suggesting its great potential for nanoelectronics.
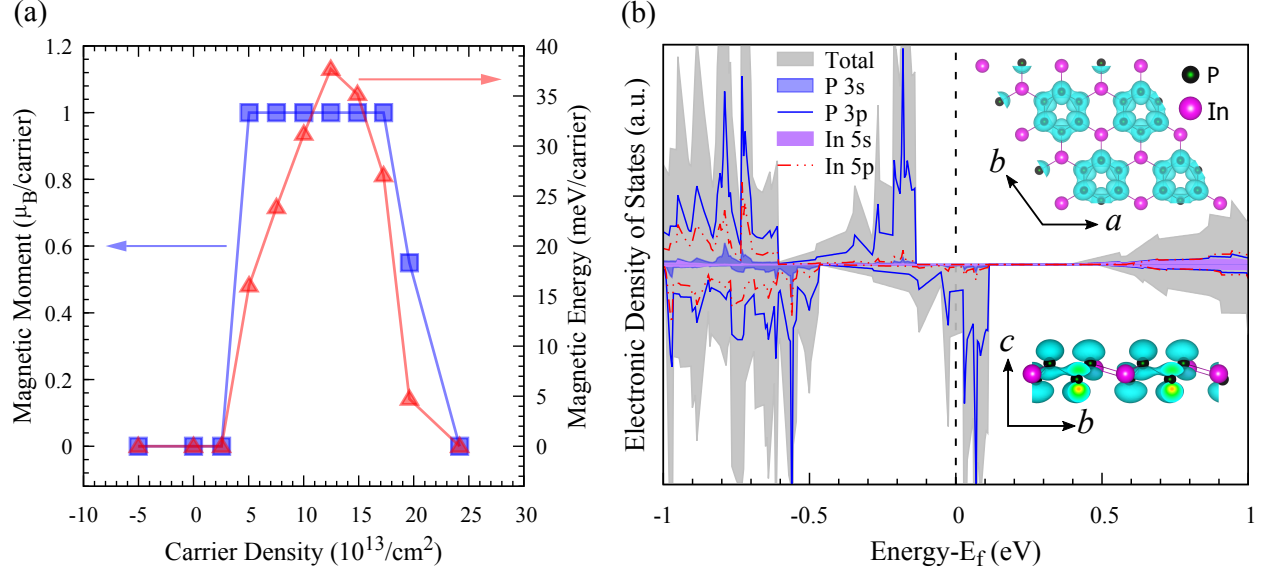
(a)

(b)

Figure 3 (a) Calculated magnetic moment and magnetic energy of InP$_3$ monolayer as a function of carrier density, where negative and positive values correspond to electron- and hole- doping densities, respectively. The magnetic energy is defined as the total energy difference between the non-magnetic and ferromagnetic states, where positive values indicate ferromagnetic state is more favourable. (b) Spin-resolved projected density of states at a hole concentration of 1.25×10^{14} cm^{-2}. The inset depicts the corresponding spin density isosurfaces. The Fermi energy is indicated by a dashed line at 0 eV.

Magnetism. Large density of states near the Fermi level is generally an indication of electronic instabilities and transitions to different phases, such as magnetism and super-conductivity.[26,58,59] As we have shown above, 2D InP$_3$ shows Mexican-hat-like bands and one-dimensional-like van Hove singularities around the Fermi energy, which is especially novel in 2D materials including graphene nanoribbons,[58] GaS, GaSe, and α-SnO monolayers.[26,58,60] In the case of InP$_3$ monolayer, we find that electronic instability can be driven by the exchange interaction from hole doping and defect engineering. Firstly, the 2D InP$_3$ crystal was doped with holes or electrons at various carrier concentrations. After full optimization of the doped cells, we calculated the magnetic moment and the magnetic energy, which is defined as the total energy difference between the non-magnetic and ferromagnetic states ($E_{Mag.} = E_{NM} - E_{FM}$). We have also tested antiferromagnetic ordering, which we find

10

to be higher in energy than ferromagnetic (Table S3 and S4). As shown in Figure 3 (a) and Table S3, the hole-doped monolayer becomes ferromagnetic (1 μ_B/carrier) and half-metallic with a large magnetic energy of 16.05 meV/carrier at a carrier density of 5.04×10^{13} cm^{-2}. The half-metallicity in hole-doped InP$_3$ monolayer is mainly dominated by the $3p$ orbital of the phosphorus atoms and the spin-density is primarily from the phosphorus along the out-of-plane direction as illustrated in Figure 3 (b). Under hole-doping, the ferromagnetic states of 2D InP$_3$ stand up to a high carrier density of 1.96×10^{14} cm^{-2} with a magnetic moment of 0.55 μ_B/carrier. The peak value of magnetic energy (37.68 meV/carrier) is observed at 1.25×10^{14} cm^{-2} with a large magnetic moment of 1 μ_B/carrier. Compared with GaSe monolayer (3 meV/carrier),[26] the highest magnetic energy of InP$_3$ monolayer is ~10 times larger, suggesting its superiority for spintronics. To obtain 2D half-metallic InP$_3$ crystal, a doping hole density from 5.04×10^{13} cm^{-2} to 1.72×10^{14} cm^{-2} can be realized experimentally by electrolyte and liquid gatings.[61,62] With the increase of hole density, the monolayer becomes metallic (Figure S4a and S4b). While, as seen from Table S3 and Figure S4e, the electron doping does not induce any magnetism in 2D InP$_3$, but resulting in a semiconductor-to-metal transition, which would be of interest for nano-sensors.

On the other hand, the ferromagnetic state in 2D InP$_3$ can also be induced by defect engineering. For instance, by replacing one P atom of InP$_3$ monolayer with Ge atom (Figure S5a), we are able to make it ferromagnetic in our simulations. As shown in Table S3, the substitution of one P with Ge atom in a $2 \times 2 \times 1$ lattice results in a magnetic moment of $1\mu_B$/cell. The corresponding magnetic energy is as high as 87.38 meV, which suggests a moderate critical temperature. Interestingly, at odd with the hole-doped 2D InP$_3$, the magnetic moment of Ge-doped InP$_3$ monolayer originates instead from the defect states around the Fermi level induced by Ge dopant (Figure S5b and S5c), including the contributions of p orbitals from In, P, and Ge atoms as well. Other elemental dopants from the IVA group, such as C, Si and Sn, may also be favourable for inducing ferromagnetism in 2D InP$_3$ monolayer. Therefore, it is expected that 2D spintronics can be achieved in atomically thin InP$_3$

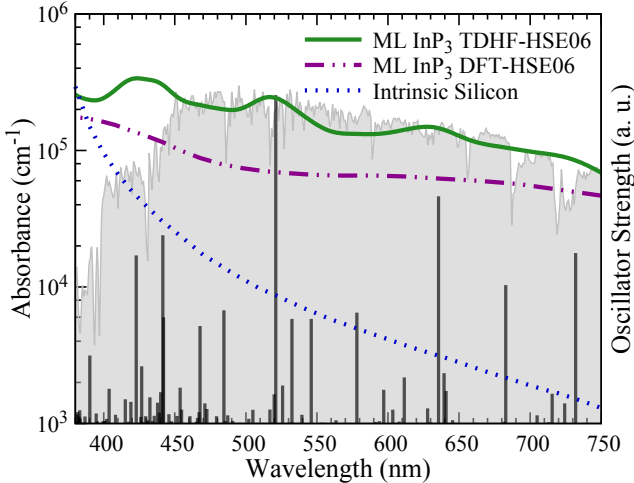monolayer from experiments by defect engineering or hole doping.

Figure 4 Calculated in-plane ($xx = yy$) absorption coefficients of 2D InP$_3$ monolayer with DFT and TDHF methods, comparing with experimental spectrum of intrinsic silicon[63] in the visible light wavelength (380-750 nm). The normalized dimensionless oscillator strength (right y axis) is depicted as black bars. The grey background indicates the reference solar spectral irradiance (Air Mass 1.5, ASTM G173-03).[64]

Absorption. The predicted InP$_3$ monolayer has a similar indirect band-gap (1.14 eV) as bulk silicon ($\sim$1.16 eV), which is an optimal gap for photovoltaic and optoelectronic applications. To assess the optical performance, we have calculated the absorption coefficients of 2D InP$_3$ crystal from the DFT/TDHF (excluding/including excitonic effect) mechods using the accurate HSE06 functional and compared with the experimentally measured absorbance of intrinsic silicon.[63] As shown in Figure 4 and Figure S6, the overall in-plane ($xx = yy$) absorption coefficients are large (10^5 cm^{-1}) and comparable to that of the organic perovskite solar cells,[65] while the out-of-plane (zz) components are small due to the typically large cross section in 2D materials. Remarkably, the predicted in-plane absorption coefficients of InP$_3$ monolayer are significantly larger than that of intrinsic silicon for most wavelengths, and the light absorbance of silicon descends dramatically above $\sim$400 nm wavelength. Furthermore, unlike silicon and many other 2D materials[23] which could only absorb light efficiently in a very narrow range of wavelengths, the 2D InP$_3$ crystal shows extraordinary light harvesting ability in the entire visible solar spectrum from 380 to 750 nm, being comparable to the MoS$_2$

monolayer[66] (Figure S6). This outstanding optical performance suggests mono-layered InP_3 crystal is a very promising material for efficient photovoltaic solar cells and optoelectronic devices.

Moreover, as illustrated in Figure 4, the absorption spectrum calculated from the TDHF-HSE06 approach is significantly higher than that from the DFT-HSE06 method, indicating large excitonic effects in many wavelengths, which enhances the absorption coefficients. The strong excitation in InP_3 monolayer may further lead to significant transfers of oscillator strength from band-to-band transitions to the fundamental exciton states with high probability of optical transitions. And the large oscillator strength of InP_3 monolayer also results in strong light-matter interactions.[67] Additionally, the strong light-matter interactions could be guaranteed by the Van Hove singularities in the electronic density of states of InP_3 monolayer, which also leads to enhanced photon absorption. This is analogous to the observation in the transition metal dichalcogenides/graphene hetrostructures, which allows development of extremely efficient flexible photovoltaic devices with a high quantum efficiency of $\sim30\%$.[68]
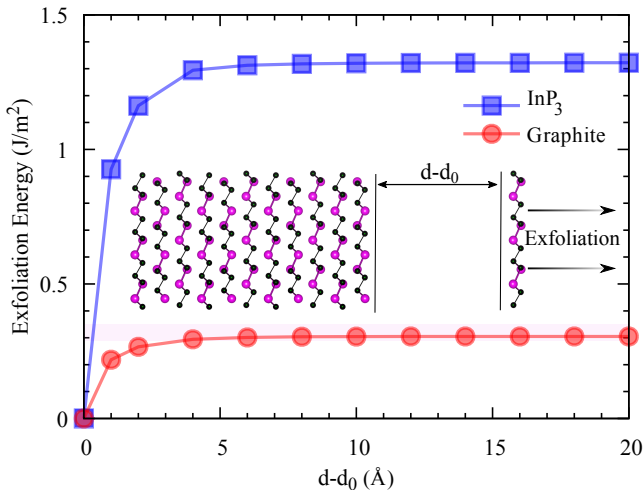

Figure 5 Calculated exfoliation energy vs separation distance d for indium triphosphide in comparison with graphite, where d_0 indicates the van der Waals gap between adjacent layers in bulk crystal.

Exfoliation. To explore the possibility of fabricating the InP_3 monolayer from the surface of its layered bulk crystal, we have simulated the exfoliation process and predicted

exfoliation energy with respect to separation as shown in Figure 5. The calculated exfoliation energy of graphite is 0.31 J/m^2, which is consistent with the experimental measurement[69] (0.32±0.03 J/m^2) and previous theoretical value[70] (0.32 J/m^2). For InP$_3$, the calculated exfoliation energy is 1.32 J/m^2, which is higher than that of graphite but in the same order of magnitude, indicating the InP$_3$ monolayer could be prepared experimentally from its bulk form using similar approaches as graphene by mechanical cleavage or liquid phase exfoliation. Nevertheless, compared to those of Ca$_2$N (1.08 J/m^2)[71] and GeP$_3$ (1.14 J/m^2),[43] the exfoliation energies of the InP$_3$ monolayer is fairly typical of 2D materials and the vdW interactions are moderate, implying its potential in constructing vdW hetrostructures for nanoelectronics.[8]
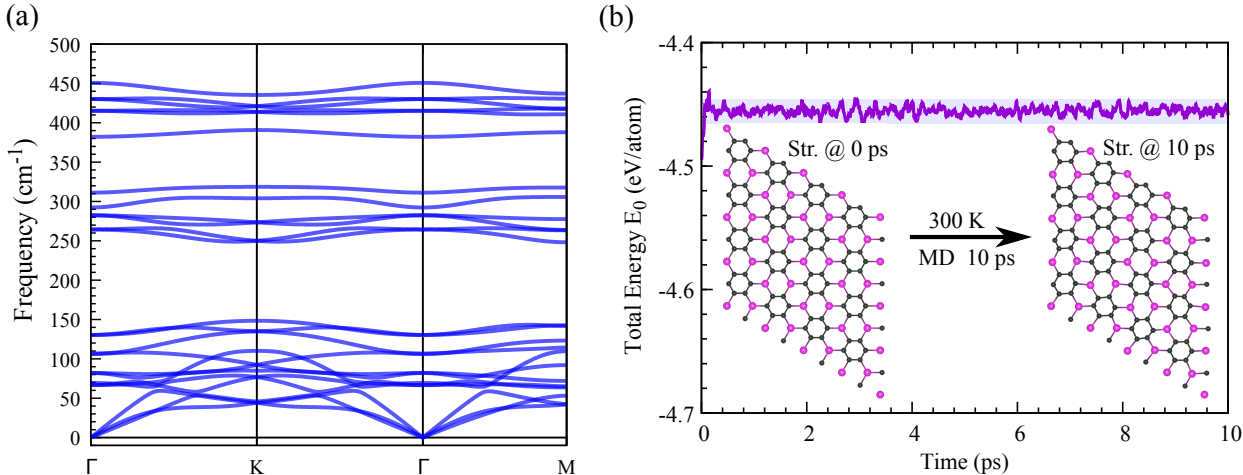

Figure 6 (a) Phonon dispersion curves of the InP$_3$ monolayer; (b) evolution of total energy and snapshots of mono-layered InP$_3$ from AIMD simulations at 0 ps and 10 ps.

Stability. The stability of 2D crystals is crucial for experimental fabrication and practical applications. The lattice dynamical stability of the InP$_3$ monolayer was assessed by calculating the phonon dispersion curves as presented in Figure 6 (a). No imaginary phonon mode is observed, indicating that 2D InP$_3$ crystal is dynamically stable. The highest frequency of optical modes reaches around 450 cm^{-1}, which is comparable to that of black phosphorene, suggesting apparent covalent P-P bondings. Moreover, to study its room-temperature thermal stability, additional *ab initio* molecular dynamics simulations have been performed at

14

300 K for the monolayer $4\times4\times1$ supercell. As indicated by the AIMD snapshots illustrated in Figure 6 (b), the planer puckered arsenic-type honeycomb networks are well maintained within 10 ps, demonstrating the InP_3 monolayer is stable at room temperature. The thermal stability of 2D InP_3 is further confirmed by the time-dependent evolution of total energies, which are oscillating within a very narrow range. All the atoms in the cell are vibrating around their equilibrium positions during the AIMD simulations and no phase transition occurs at 300 K temperature.

CONCLUSIONS

In summary, we have theoretically predicted a new 2D semiconductor InP_3 which shows various exceptional electronic properties. The mono-layered InP_3 has a weakly indirect band-gap (1.14 eV) and exhibits high electron mobility (1919 $cm^2V^{-1}s^{-1}$). Interestingly, we found that 2D InP_3 crystal shows electronic instabilities in its band structure, *i.e.*, Mexican-hat-like flat bands and van Hove singularities near the Fermi energy, which result in a non-monotonic electronic response to compressive and tensile strains. Thanks to the novel band features, robust ferromagnetic and half-metallic states can be induced and tuned by p-type doping (hole concentration from 5.04×10^{13} to 1.72×10^{14} cm^{-2}) or defect engineering (substitution of P atom with Ge) in mono-layered InP_3. These ferromagnetic half-metallic states, giving rise to 100% spin-polarized currents, could be achieved readily from experiments by electrolyte and liquid gatings or substitution of phosphorus with germanium atom. A semiconductor-metal transition is also revealed in the InP_3 monolayer under electron or high-concentration hole doping. In addition, the InP_3 monolayer possesses extraordinary optical absorbance (10^5 cm^{-1}) with significant excitonic effects in the entire visible solar spectrum, which is better than intrinsic silicon and comparable to mono-layered MoS_2. Finally, as demonstrated, the proposed InP_3 monolayer shows good lattice dynamical and thermal stability and is expected to be fabricated experimentally from its layered bulk crystal by exfoliation. These favourable

features promote the investigated 2D InP$_3$ crystal as a promising candidate for nano-scale electronic, photovoltaic, and spintronic applications. We believe our work will stimulate the fabrication and investigation of 2D InP$_3$ crystal in the near future.

Supporting Information Available

The following files are available free of charge.

- Table S1: Calculated structural properties of bulk InP$_3$ in comparison with experiments. Table S2: Calculated lattice parameters, bond lengths, and bond angles of bulk and mono-layered InP$_3$. Table S3: Calculated magnetic and structural properties of electron-, hole-, and Ge-doped InP$_3$ monolayer. Table S4: Calculated total energy of the hole-doped InP$_3$ monolayer with different magnetic orders at the carrier concentration of 1.25×10^{14} cm^{-2}. Figure S1: Electronic band structures of bi-layered and tri-layered InP$_3$. Figure S2: Calculated electronic density of states of the InP$_3$ monolayer with/without surface relaxation. Figure S3: Calculated electronic band edges of mono-layered InP$_3$ with orthogonal cells under various strains. Figure S4: Spin-resolved projected electronic density of states of the InP$_3$ monolayer at various hole-doping concentrations. Figure S5: Structural configuration and spin-resolved projected electronic density of states of Ge-doped InP$_3$ monolayer. Figure S6: In-plane and out-of-plane absorption coefficients from TDHF-HSE06 calculations. Figure S7: Various anti-ferromagnetic configurations with orientated up (↑) and down (↓) spins on phosphorus (germanium) atoms being considered in this work.

Acknowledgement

References

(1) Novoselov, K. S.; Geim, A. K.; Morozov, S.; Jiang, D.; Zhang, Y.; Dubonos, S.; Grigorieva, I.; Firsov, A. *Science* **2004**, *306*, 666–669.

(2) Novoselov, K.; Geim, A. K.; Morozov, S.; Jiang, D.; Katsnelson, M.; Grigorieva, I.; Dubonos, S.; Firsov, A. *Nature* **2005**, *438*, 197–200.

(3) Geim, A. K.; Novoselov, K. S. *Nat. Mater.* **2007**, *6*, 183–191.

(4) Zhang, Z.; Liu, X.; Yakobson, B. I.; Guo, W. *J. Am. Chem. Soc.* **2012**, *134*, 19326–19329.

(5) Koski, K. J.; Cui, Y. *ACS Nano* **2013**, *7*, 3739–3743.

(6) Xu, M.; Liang, T.; Shi, M.; Chen, H. *Chem. Rev.* **2013**, *113*, 3766–3798.

(7) Li, X.; Wu, X.; Yang, J. *J. Am. Chem. Soc.* **2014**, *136*, 11065–11069.

(8) Tan, C.; Zhang, H. *J. Am. Chem. Soc.* **2015**, *137*, 12162–12174.

(9) Yang, L.-M.; Bacic, V.; Popov, I. A.; Boldyrev, A. I.; Heine, T.; Frauenheim, T.; Ganz, E. *J. Am. Chem. Soc.* **2015**, *137*, 2757–2762.

(10) Yoo, Y.; Degregorio, Z. P.; Johns, J. E. *J. Am. Chem. Soc.* **2015**, *137*, 14281–14287.

(11) Zhang, H.; Li, Y.; Hou, J.; Tu, K.; Chen, Z. *J. Am. Chem. Soc.* **2016**, *138*, 5644–5651.

(12) Zhuo, Z.; Wu, X.; Yang, J. *J. Am. Chem. Soc.* **2016**, *138*, 7091–7098.

(13) Deng, D.; Novoselov, K.; Fu, Q.; Zheng, N.; Tian, Z.; Bao, X. *Nat. Nanotechnol.* **2016**, *11*, 218–230.

(14) Cahangirov, S.; Topsakal, M.; Aktürk, E.; Şahin, H.; Ciraci, S. *Phys. Rev. Lett.* **2009**, *102*, 236804.

(15) Zhao, J.; Liu, H.; Yu, Z.; Quhe, R.; Zhou, S.; Wang, Y.; Liu, C. C.; Zhong, H.; Han, N.; Lu, J.; Yao, Y.; Wu, K. *Prog. Mater Sci.* **2016**, *83*, 24–151.

(16) Li, L.; Yu, Y.; Ye, G. J.; Ge, Q.; Ou, X.; Wu, H.; Feng, D.; Chen, X. H.; Zhang, Y. *Nat. Nanotechnol.* **2014**, *9*, 372–377.

(17) Qiao, J.; Kong, X.; Hu, Z.-X.; Yang, F.; Ji, W. *Nat. Commun.* **2014**, *5*, 4475.

(18) Naguib, M.; Kurtoglu, M.; Presser, V.; Lu, J.; Niu, J.; Heon, M.; Hultman, L.; Gogotsi, Y.; Barsoum, M. W. *Adv. Mater.* **2011**, *23*, 4248–4253.

(19) Tang, Q.; Zhou, Z.; Shen, P. *J. Am. Chem. Soc.* **2012**, *134*, 16909–16916.

(20) Naguib, M.; Mochalin, V. N.; Barsoum, M. W.; Gogotsi, Y. *Adv. Mater.* **2014**, *26*, 992–1005.

(21) Ayari, A.; Cobas, E.; Ogundadegbe, O.; Fuhrer, M. S. *J. Appl. Phys.* **2007**, *101*, 14507–14507.

(22) Mak, K. F.; Lee, C.; Hone, J.; Shan, J.; Heinz, T. F. *Phys. Rev. Lett.* **2010**, *105*, 136805.

(23) Wang, Q. H.; Kalantar-Zadeh, K.; Kis, A.; Coleman, J. N.; Strano, M. S. *Nat. Nanotechnol.* **2012**, *7*, 699–712.

(24) Island, J. O.; Barawi, M.; Biele, R.; Almazán, A.; Clamagirand, J. M.; Ares, J. R.; Sánchez, C.; van der Zant, H. S.; Álvarez, J. V.; D'Agosta, R.; Ferrer, I. J.; Castellanos-Gomez, A. *Adv. Mater.* **2015**, *27*, 2595–2601.

(25) Dai, J.; Zeng, X. C. *Angew. Chem.* **2015**, *127*, 7682–7686.

(26) Cao, T.; Li, Z.; Louie, S. G. *Phys. Rev. Lett.* **2015**, *114*, 236602.

(27) Hu, T.; Wu, H.; Zeng, H.; Deng, K.; Kan, E. *Nano Lett.* **2016**, *16*, 8015–8020.

(28) Zhang, S.; Yan, Z.; Li, Y.; Chen, Z.; Zeng, H. *Angew. Chem. Int. Ed.* **2015**, *54*, 3112–3115.

(29) Du, K.-Z.; Wang, X.-Z.; Liu, Y.; Hu, P.; Utama, M. I. B.; Gan, C. K.; Xiong, Q.; Kloc, C. *ACS Nano* **2016**, *10*, 1738–1743.

(30) Liu, H.; Neal, A. T.; Zhu, Z.; Luo, Z.; Xu, X.; Tománek, D.; Ye, P. D. *ACS Nano* **2014**, *8*, 4033–4041.

(31) Kinomura, N.; Terao, K.; Kikkawa, S.; Horiuchi, H.; Koizumi, M.; Setoguchi, H. *Mater. Res. Bull.* **1983**, *18*, 53–57.

(32) Gullman, J.; Olofsson, O. *J. Solid State Chem.* **1972**, *5*, 441–445.

(33) Blochl, P. E. *Phys. Rev. B* **1994**, *50*, 17953.

(34) Hafner, J. *J. Comput. Chem.* **2008**, *29*, 2044–2078.

(35) Perdew, J. P.; Burke, K.; Ernzerhof, M. *Phys. Rev. Lett.* **1996**, *77*, 3865.

(36) Grimme, S.; Antony, J.; Ehrlich, S.; Krieg, H. *J. Chem. Phys.* **2010**, *132*, 154104.

(37) Paier, J.; Marsman, M.; Hummer, K.; Kresse, G.; Gerber, I. C.; Ángyán, J. G. *J. Chem. Phys.* **2006**, *124*, 154709.

(38) Kresse, G.; Furthmüller, J.; Hafner, J. *EPL* **1995**, *32*, 729.

(39) Parlinski, K.; Li, Z. Q.; Kawazoe, Y. *Phys. Rev. Lett.* **1997**, *78*, 4063–4066.

(40) Togo, A.; Tanaka, I. *Scripta Mater.* **2015**, *108*, 1–5.

(41) Bardeen, J.; Shockley, W. *Phys. Rev.* **1950**, *80*, 72.

(42) Guo, Z.; Zhou, J.; Zhu, L.; Sun, Z. *J. Mater. Chem.A* **2016**, *4*, 11446–11452.

(43) Jing, Y.; Ma, Y.; Li, Y.; Heine, T. *Nano Lett.* **2017**, *17*, 1833–1838.

(44) Fonari, A.; Sutton, C. Effective Mass Calculator for Semiconductors. 2015.

(45) Paier, J.; Marsman, M.; Kresse, G. *Phys. Rev. B* **2008**, *78*, 121201.

(46) Saha, S.; Sinha, T.; Mookerjee, A. *Phys. Rev. B* **2000**, *62*, 8828.

(47) King-Smith, R.; Vanderbilt, D. *Phys. Rev. B* **1993**, *47*, 1651.

(48) Gajdoš, M.; Hummer, K.; Kresse, G.; Furthmüller, J.; Bechstedt, F. *Phys. Rev. B* **2006**, *73*, 045112.

(49) Nosé, S. *J. Chem. Phys.* **1984**, *81*, 511–519.

(50) Hoover, W. G. *Phys. Rev. A* **1985**, *31*, 1695.

(51) Zheng, F.; Tan, L. Z.; Liu, S.; Rappe, A. M. *Nano Lett.* **2015**, *15*, 7794–7800.

(52) ODonnell, K.; Chen, X. *Appl. Phys. Lett.* **1991**, *58*, 2924–2926.

(53) Becke, A. D.; Edgecombe, K. E. *J. Chem. Phys.* **1990**, *92*, 5397–5403.

(54) Silvi, B.; Savin, A. *Nature* **1994**, *371*, 683–686.

(55) Sun, Y.; Thompson, S. E.; Nishida, T. *J. Appl. Phys.* **2007**, *101*, 104503.

(56) Conley, H. J.; Wang, B.; Ziegler, J. I.; Haglund, R. F.; Pantelides, S. T.; Bolotin, K. I. *Nano Lett.* **2013**, *13*, 3626–3630.

(57) Fei, R.; Yang, L. *Nano Lett.* **2014**, *14*, 2884–2889.

(58) Son, Y.-W.; Cohen, M. L.; Louie, S. G. *Nature* **2006**, *444*, 347–349.

(59) Bristowe, N.; Stengel, M.; Littlewood, P.; Artacho, E.; Pruneda, J. *Phys. Rev. B* **2013**, *88*, 161411.

(60) Seixas, L.; Rodin, A.; Carvalho, A.; Neto, A. C. *Phys. Rev. Lett.* **2016**, *116*, 206803.

(61) Efetov, D. K.; Kim, P. *Phys. Rev. Lett.* **2010**, *105*, 256805.

(62) Zhang, Y.; Oka, T.; Suzuki, R.; Ye, J.; Iwasa, Y. *Science* **2014**, *344*, 725–728.

(63) Green, M. A.; Keevers, M. J. *Prog. Photovoltaics Res. Appl.* **1995**, *3*, 189–192.

(64) G173-03, A. Standard Tables for Reference Solar Spectral Irradiances: Direct Normal and Hemispherical on 37 Tilted Surface, ASTM International, West Conshohocken, PA, 2012,. `https://doi.org/10.1520/G0173-03R12`.

(65) Shirayama, M.; Kadowaki, H.; Miyadera, T.; Sugita, T.; Tamakoshi, M.; Kato, M.; Fujiseki, T.; Murata, D.; Hara, S.; Murakami, T. N.; Fujimoto, S.; Chikamatsu, M.; Fujiwara, H. *Phys. Rev. Appl.* **2016**, *5*, 014012.

(66) Liu, H.-L.; Shen, C.-C.; Su, S.-H.; Hsu, C.-L.; Li, M.-Y.; Li, L.-J. *Appl. Phys. Lett.* **2014**, *105*, 201905.

(67) Mak, K. F.; Shan, J. *Nat. Photonics* **2016**, *10*, 216–226.

(68) Britnell, L.; Ribeiro, R. M.; Eckmann, A.; Jalil, R.; Belle, B. D.; Mishchenko, A.; Kim, Y.-J.; Gorbachev, R. V.; Georgiou, T.; Morozov, S. V.; Grigorenko, A. N.; Geim, A. K.; Casiraghi, C.; Neto, A. H. C.; Novoselov, K. S. *Science* **2013**, *340*, 1311–1314.

(69) Zacharia, R.; Ulbricht, H.; Hertel, T. *Phys. Rev. B* **2004**, *69*, 155406.

(70) Ziambaras, E.; Kleis, J.; Schröder, E.; Hyldgaard, P. *Phys. Rev. B* **2007**, *76*, 155425.

(71) Zhao, S.; Li, Z.; Yang, J. *J. Am. Chem. Soc.* **2014**, *136*, 13313–13318.

Graphical TOC Entry